PAPER

Check for updates

Tuning the coordination number of Fe single atoms for the efficient reduction of CO_2†

Huihuang Chen, ‡[a] Xu Guo,‡[a] Xiangdong Kong,[a] Yulin Xing,[a] Yan Liu,[a] Bolong Yu,[a] Qun-Xiang Li, [a] Zhigang Geng,*[a] Rui Si *[b] and Jie Zeng *[a]

CO_2 electroreduction into valuable products holds great promise for energy supply and environmental remediation but remains a challenge due to the lack of high-performance electrocatalysts. Herein, we developed an efficient strategy to prepare highly active Fe single-atom catalysts ($Fe-N_5/Fe-N_6$) by tuning the coordination number of Fe with N towards CO_2 electroreduction. The faradaic efficiency of CO for $Fe-N_5$ exceeded 90% ranging from −0.35 to −0.65 V *versus* the reversible hydrogen electrode (*vs*. RHE) towards CO_2 electroreduction. The turnover frequency of CO for $Fe-N_5$ reached 5006 h^{-1} at −1.05 V *vs*. RHE, which was 3.8 times that (1324 h^{-1}) of $Fe-N_6$. Besides, CO was generated at an overpotential as low as 50 mV over $Fe-N_5$, smaller than that (90 mV) over $Fe-N_6$. Density functional theory calculations demonstrated that $Fe-N_5$ facilitated the adsorption and activation of CO_2 to form the *COOH intermediate, thus leading to superior selectivity and activity for CO_2 electroreduction.

1. Introduction

The ever-increasing combustion of depletable fossil fuels has resulted in a serious energy crisis and environmental pollution worldwide due to the massive release of atmospheric carbon dioxide (CO_2).[1,2] CO_2 electroreduction into value-added carbon products is considered as an ideal approach to mitigate the energy and environmental issues.[3,4] To achieve high energy efficiency and feasible scalability, the reaction must occur rapidly and selectively at low overpotentials. However, this technology is still hindered by the high overpotential, low activity, and limited product selectivity of electrocatalysts nowadays, arising from the chemical inertness of linear CO_2 and the thermodynamically favorable competing hydrogen evolution reaction.[5–12] To overcome these drawbacks, it is crucial to develop efficient and robust catalysts towards CO_2 electroreduction.

Carbon monoxide (CO) has emerged as one of the most practical products of CO_2 electroreduction owing to its indis-

pensable role in the preparation of synthetic liquid fuels *via* the industrial Fischer–Tropsch process.[13] The benchmark electrocatalysts for the CO_2-to-CO conversion are Ag- and Au-based materials, which demonstrated over 90% faradaic efficiency for CO formation with an overpotential of 240 mV,[14–16] but their high price, scarcity and inadequate activity warrant further research endeavors to explore low-cost and Earth-abundant nonprecious-metal catalysts to replace those noble-metal catalysts. Recently, single-atom catalysts (SACs) have been identified as promising candidates in the field of electrochemical conversion processes.[17–21] This is because the unique features of SACs such as tailorable electronic structure, maximized atomic utilization, and unsaturated coordination environment render them intriguing properties for catalysis dramatically different from their bulk counterparts.[22] To this end, various strategies (*e.g.* defect engineering, structural manipulation, and interfacial regulation) have been proposed to develop nonprecious-metal (Fe, Co, Ni, and Sb) SACs for the CO_2-to-CO conversion.[23–31] Nevertheless, their electrocatalytic performance still suffers from either the large overpotential or the tradeoff between high faradaic efficiency and appreciable current density.[32–34] Typically, the faradaic efficiency of CO_2 electroreduction drops rapidly with increasing potential in order to deliver reasonable current density. In such a context, it remains a challenge to develop robust nonprecious-metal SACs to address the aforementioned two limitations for the practical implementation of CO_2 electroreduction.

Herein, we developed an efficient strategy to prepare highly active Fe SACs ($Fe-N_5/Fe-N_6$) by tuning the coordination number of Fe with N towards CO_2 electroreduction. The mass

[a]*Hefei National Laboratory for Physical Sciences at the Microscale, CAS Key Laboratory of Strongly-Coupled Quantum Matter Physics, Key Laboratory of Surface and Interface Chemistry and Energy Catalysis of Anhui Higher Education Institutes, Department of Chemical Physics, University of Science and Technology of China, Hefei, Anhui 230026, P. R. China. E-mail: gengzg@ustc.edu.cn, zengj@ustc.edu.cn*
[b]*Shanghai Synchrotron Radiation Facility, Shanghai Institute of Applied Physics, Chinese Academy of Sciences, Shanghai 201204, P. R. China.*
E-mail: sirui@sinap.ac.cn
†Electronic supplementary information (ESI) available: Figures, tables and methods related to this article. See DOI: 10.1039/d0gc02689a
‡These authors contributed equally to this work.

loading of Fe in Fe–N$_5$ and Fe–N$_6$ was determined to be 0.57% and 0.58%, respectively, by inductively coupled plasma atomic emission spectroscopy (ICP-AES). The faradaic efficiency (FE) of CO (FE$_{CO}$) for Fe–N$_5$ exceeded 90% within a wide potential window from −0.35 to −0.65 V *versus* the reversible hydrogen electrode (*vs.* RHE). Meanwhile, the turnover frequency (TOF) of CO (TOF$_{CO}$) for Fe–N$_5$ reached 5006 h^{-1} at −1.05 V *vs.* RHE, which was 3.8 times as high as that (1324 h^{-1}) for Fe–N$_6$. Besides, CO was generated at an overpotential as low as 50 mV over Fe–N$_5$, smaller than that (90 mV) over Fe–N$_6$. Experimental results and density functional theory (DFT) calculations demonstrated that Fe–N$_5$ facilitated the adsorption and activation of CO$_2$ to form the key *COOH intermediate, thus leading to the superior selectivity and activity for CO$_2$ electroreduction. Our findings highlight the significance of regulating the coordination number of active centers in SACs to simultaneously enhance the catalytic activity and selectivity towards CO$_2$ electroreduction.

2. Experimental methods

2.1. Materials and chemicals

Anhydrous ferric chloride (FeCl$_3$, 99%, Sigma), zinc nitrate hexahydrate (Zn(NO$_3$)$_2$·6H$_2$O, 99%, Aladdin), 2-methylimidazole (2-mIm, 99%, Sigma), potassium hydroxide (KOH, 99%, Sinopharm Chemical Reagent Co. Ltd. (Shanghai, China)), potassium bicarbonate (KHCO$_3$, 99%, Sigma), iron nanoparticles (Fe NPs, 99%, Sigma), ferric oxide (Fe$_2$O$_3$, 99%, Sigma), ferriferrous oxide (Fe$_3$O$_4$, 99%, Sigma), methanol (99.8%, Fisher), and ethanol (99.8%, Fisher) were used as received without further purification. Carbon paper, Nafion 115 membrane, and Nafion solution (5% wt%) were supplied by Sigma-Aldrich. Ultrapure Millipore water (18.2 MΩ cm, Milli-Q, Millipore Co.) was used in all experiments.

2.2. Preparation of catalysts

In a typical synthetic process of Fe-doped ZIF-8, 0.09 g of FeCl$_3$ and 5.03 g of Zn(NO$_3$)$_2$·6H$_2$O were dissolved in 480 mL of methanol containing 11.1 g of 2-mIm. Then the mixture was kept at 25 °C for 12 h. The resultant solid products were separated by centrifugation and thoroughly washed with methanol five times, followed by drying at 60 °C under vacuum overnight. The synthetic procedure of ZIF-8 was the same as the above except no FeCl$_3$ was introduced. The as-obtained Fe-doped ZIF-8 was placed in a tube furnace and pyrolyzed (900 °C for Fe–N$_5$, 800 °C for Fe–N$_6$) for 6 hours with a heating rate of 5 °C min^{-1} under an Ar flow (100 mL min^{-1}). After naturally cooling to room temperature, Fe–N$_5$ and Fe–N$_6$ were obtained as black powder and directly used without any further treatment. The synthetic process of pyrolyzed ZIF-8 was the same with Fe–N$_5$/Fe–N$_6$ except that the precursor was pure ZIF-8 instead of Fe-doped ZIF-8. Pyrolyzed ZIF-8 at 800 and 900 °C is denoted as ZIF-8-800 and ZIF-8-900, respectively.

2.3. Electrochemical measurements

All electrochemical experiments were carried out on a CHI760E electrochemical workstation (CHI660E, Shanghai CHI Instruments Company) at atmospheric pressure and ambient temperature. In a typical preparation procedure of the working electrode, 3 mg of the catalyst and 37 μL of Nafion solution was dispersed in 2.0 ml of water–ethanol solution with a volume ratio of 1 : 3, followed by sonication for 1 hour to obtain the homogeneous catalyst ink. The ink was then uniformly loaded onto one side of carbon paper with an area of 2 × 2 cm^2, which was directly used for the electrochemical measurements after drying. A flow-cell was used as the electrolyzer for CO$_2$ electrochemical reduction in 1.0 M KOH. The cathodic chamber and anodic chamber were separated by a proton exchange membrane (Nafion 115). A mass flow controller was used to set the CO$_2$ flow gas at 10 sccm. The deposited carbon paper, Pt wire, and Ag/AgCl served as the working electrode, counter electrode, and reference electrode, respectively. All potentials reported in this study were *vs.* RHE *via* the equation $E(vs.\text{ RHE}) = E(vs.\text{ Ag/AgCl}) + 0.197\text{ V} + 0.0592 \times \text{pH}$. The pH value of the electrolyte was determined with a Mettler Toledo FE 28 Desktop pH meter (Mettler Toledo International Inc., Shanghai, China). Controlled potential electrolysis was performed at each potential for 40 min. The current density was normalized with the geometric surface area of the carbon paper. Cyclic voltammetry measurements of Fe–N$_5$ and Fe–N$_6$ were carried out from 1.08 to 1.18 V *vs.* RHE and 1.06 to 1.16 V *vs.* RHE at various scan rates under a CO$_2$ atmosphere to obtain the double layer capacitance (C_{dl}). The C_{dl} was determined by plotting the current density difference Δj ($j_a - j_c$) at 1.13 and 1.11 V *vs.* RHE against the scan rates, where j_a and j_c represent the anodic and cathodic current density, respectively. The C_{dl} is half of the linear slope and positively correlated with the electrochemical active surface area.

2.4. Determination of reduction products

The products of CO$_2$ electrochemical reduction were determined by gas chromatography (GC) and nuclear magnetic resonance (NMR) spectroscopy. Particularly, the gas products were monitored by an online gas chromatgraph (Shimadzu 2010 plus GC) equipped with a thermal conductivity detector (TCD) and Molsieve 5 A column every five minutes. The liquid products were analyzed using BRUKER AVANCE III HD 400 NMR by mixing 0.5 mL of electrolyte after electrolysis, 0.1 mL of deuterium oxide (D$_2$O) and 0.1 mL of 6 mM1-propanesulfonic acid 3-(trimethylsilyl) sodium salt (DSS) solution. CO and H$_2$ are the only two gas products and no liquid products are detected after electrolysis for both Fe–N$_5$ and Fe–N$_6$.

3. Results and discussion

3.1. Structural characterization

Fe–N$_5$ and Fe–N$_6$ were obtained *via* pyrolyzing an Fe-containing derivative of zeolitic imidazolate framework-8 (ZIF-8) at

Fig. 1 (a) Schematic of the formation process of Fe−N_6 and Fe−N_5. (b) SEM, (c) TEM, and (d) HAADF-STEM images of Fe−N_5. (e) and (f) Magnified HAADF-STEM images of Fe−N_5 demonstrate the atomic dispersion of Fe atoms. (g) EDS elemental mapping reveals the homogeneous distribution of Fe, N, and C in Fe−N_5.

900 and 800 °C, respectively. The synthetic scheme of Fe−N_5 and Fe−N_6 is illustrated in Fig. 1a. The Fe-containing derivative of ZIF-8 was synthesized through the standard synthetic route of ZIF-8 except for partially substituting $Zn(NO_3)_2$ with $FeCl_3$. As shown by transmission electron microscopy (TEM) images, the Fe-containing derivative of ZIF-8 exhibited a homogeneous rhombododecahedral morphology with an average size of 220 nm (Fig. S1†). Scanning electron microscopy (SEM), TEM, and aberration-corrected high-angle annular dark-field scanning transmission electron microscopy (HAADF-STEM) images of Fe−N_5 suggested that the original structure of the Fe-containing derivative of ZIF-8 shrank into regular microporous rhombododecahedra with an average size of 200 nm after the pyrolysis process (Fig. 1b–d). Magnified HAADF-STEM images of Fe−N_5 clearly demonstrated that individual Fe atoms were uniformly dispersed in the microporous frame (Fig. 1e and f). Energy-dispersive X-ray spectroscopy (EDS) elemental mapping of Fe−N_5 displayed the homogeneous distribution of C, N, and Fe over the entire architecture (Fig. 1g). Compared with Fe−N_5,

Fe−N_6 displayed a similar morphology and elemental composition (Fig. S2†).

To gain insights into the structure and composition information of Fe−N_5 and Fe−N_6, we conducted a series of characterization techniques. The X-ray diffraction (XRD) patterns of Fe−N_5 and Fe−N_6 exhibited two broad peaks at 24.1° and 43.3°, which can be assigned to the (002) and (101) facets of graphite carbon, respectively (Fig. 2a).[8] No characteristic peaks of Fe or FeO_x crystals appeared in the XRD patterns of Fe−N_5 and Fe−N_6, which further demonstrated that Fe species were atomic Fe in Fe−N_5 and Fe−N_6. As displayed in Fig. 2b, the N $1s$ spectra of Fe−N_5 and Fe−N_6 were deconvoluted into four distinct peaks at 398.6, 399.7, 400.9, and 402.3 eV, which could be assigned to pyridinic N, Fe−N, pyrrolic N, and graphitic N, respectively.[35,36] Notably, the fraction of Fe−N decreased from 15.16% for Fe−N_6 to 8.44% for Fe−N_5, indicating that the elevated temperature reduced the coordination number of Fe with N (Table S1†). We further carried out Raman measurements to study the structure difference between Fe−N_5 and Fe−N_6. As shown in
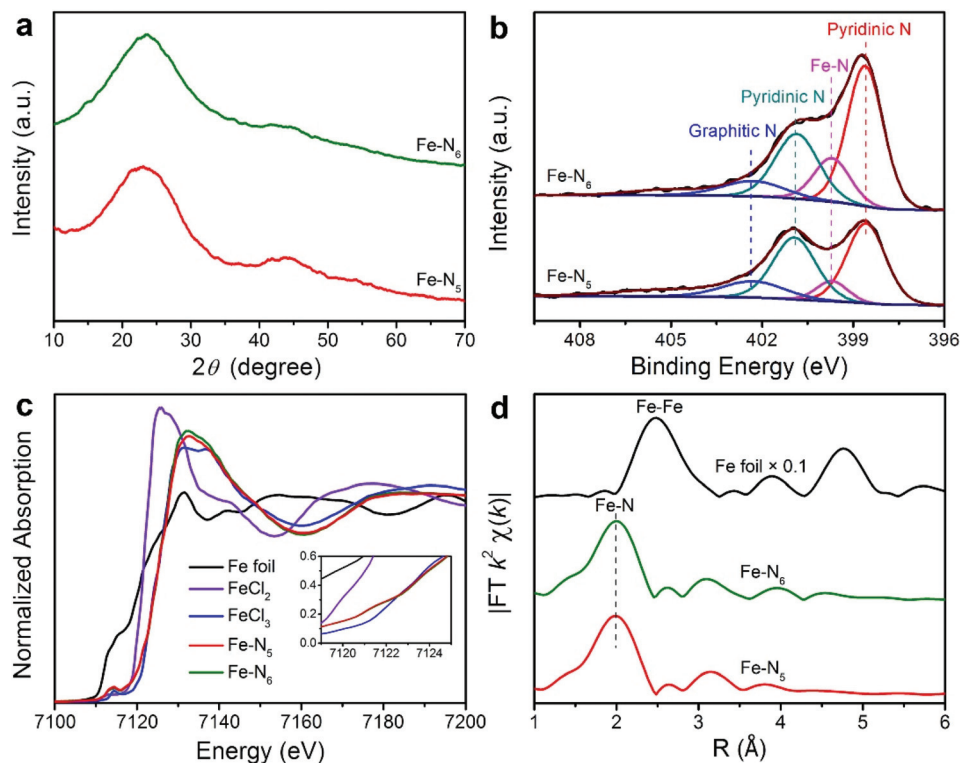
Fig. 2 (a) XRD patterns of Fe–N_5 and Fe–N_6. (b) High-resolution N 1s XPS spectra of Fe–N_5 and Fe–N_6. (c) Fe K-edge XANES spectra of Fe–N_5, Fe–N_6 and Fe foil/$FeCl_2$/$FeCl_3$ reference materials. (d) Fe K-edge k^2-weighted FT-EXAFS spectra of Fe–N_5, Fe–N_6, and Fe foil.

Fig. S3,† two peaks at 1350 and 1585 cm^{-1} are assigned to the D band and G band of graphite carbon, respectively.[37,38] The intensity ratio of D band to G band (I_D/I_G) for Fe–N_5 is 0.99, which is lower than that (1.02) for Fe–N_6. This implies that a higher temperature enhanced the graphitization of carbon in Fe–N_5. To further investigate the electronic and coordination structure of Fe–N_5 and Fe–N_6, we conducted X-ray absorption fine structure (XAFS) spectroscopy measurements. Fig. 2c shows the Fe K-edge X-ray absorption near-edge structure (XANES) profiles for Fe–N_5, Fe–N_6, $FeCl_2$, $FeCl_3$, and Fe foil. Fe–N_5 and Fe–N_6 exhibited similar energy absorption edge profiles with $FeCl_3$ in the energy range between 7120 and 7124 eV, indicating that the valence state of Fe species in both Fe–N_5 and Fe–N_6 was *ca.* +3. As shown in Fig. 2d, the extended X-ray absorption fine structure (EXAFS) spectra of both Fe–N_5 and Fe–N_6 exhibited only one prominent peak at approximately 2.0 Å, which could be attributed to Fe–N bonds. No significant contribution of the Fe–Fe bond was observed at 2.49 Å, further revealing the atomic dispersion of Fe atoms throughout the whole Fe–N_5 and Fe–N_6 structure. We also conducted a least-squares EXAFS fitting. When the EXAFS fitting parameter of bond length was set to 2.00 Å with the coordination number of *ca.* 5.4 and 6.0 for Fe–N_5 and Fe–N_6, respectively, the fitting curves of Fe–N_5 and Fe–N_6 perfectly matched with the EXAFS result (Table S2 and Fig. S4†). The coordination number of Fe with N decreased when increasing the pyrolysis temperature from 800 to 900 °C, which is due to the fact that more Fe^{III}-imi-

dazolate-Fe^{III} linkages would decompose to release CN fragments at elevated temperatures, thus resulting in the decay of Fe–N bonds.

3.2. Electrocatalytic performance towards CO_2 electroreduction

We used a flow-cell system with 1.0 M KOH as the electrolyte to evaluate the electrocatalytic performance of Fe–N_5 and Fe–N_6 towards CO_2 electroreduction (Fig. S5†). During the process of chronoamperometry electrolysis, the gaseous products of H_2 and CO were quantified *via* online gas chromatograph (GC) (Fig. S6a†). Meanwhile, no liquid products were detected in the cathodic electrolyte *via* ^{1}H nuclear magnetic resonance (^{1}H NMR) (Fig. S6b†). Fe–N_5 demonstrated a significantly higher reduction current density than Fe–N_6 throughout the potential range based on the cyclic voltammograms (CVs), indicating the superior electrocatalytic performance of Fe–N_5 compared to Fe–N_6 (Fig. S7†). Fig. 3a shows the FE_{CO} of Fe–N_5 and Fe–N_6 at various applied potentials. Fe–N_5 exhibited a higher FE_{CO} than Fe–N_6 at each applied potential. In particular, the FE_{CO} of Fe–N_5 was higher than 90% within a wide electrochemical window from −0.35 to −0.65 V *vs.* RHE. Note that the FE_{CO} of Fe–N_5 reached nearly 100% (99%) at −0.35 V *vs.* RHE. More importantly, CO was already detected at a low potential of −0.16 and −0.20 V *vs.* RHE for Fe–N_5 and Fe–N_6, respectively (Fig. S8†). Considering the CO_2/CO equilibrium potential is −0.11 V *vs.* RHE, the overpotential to produce CO was merely
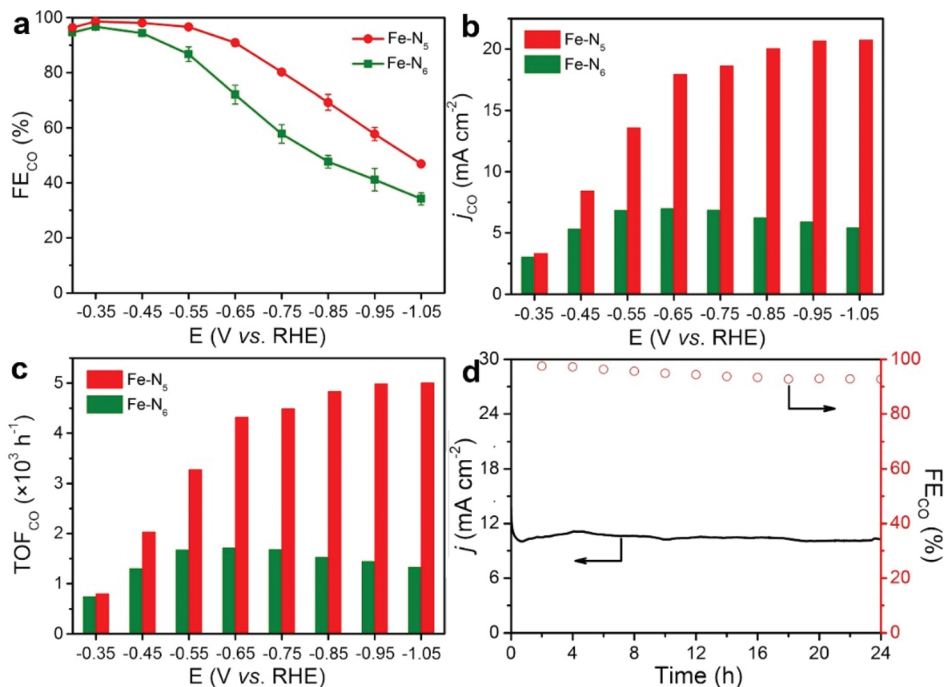
Fig. 3 CO_2 electroreduction catalytic performance of Fe–N_5 and Fe–N_6. (a) Faradaic efficiency of CO at different potentials. (b) j_{CO} in 1.0 M KOH electrolyte. (c) TOF_{CO} at various applied potentials. (d) 24 h stability test of Fe–N_5 at −0.4 V vs. RHE and the corresponding FE_{CO}.

50 and 90 mV for Fe–N_5 and Fe–N_6, respectively, even outperforming that for noble-metal catalysts such as Ag and Au.[39–43] Fig. 3b shows the partial current density of CO (j_{CO}) of Fe–N_5 and Fe–N_6. Fe–N_5 exhibited higher j_{CO} at all applied potentials. At −1.05 V vs. RHE, the j_{CO} of Fe–N_5 was up to −20.8 mA cm^{-2}, which was 3.8 times as high as that for Fe–N_6. The C_{dl} (2.58 mF cm^{-2}) of Fe–N_5 was close to that (2.25 mF cm^{-2}) of Fe–N_6 (Fig. S9†), implying that Fe–N_5 and Fe–N_6 possessed comparable electrochemical active surface area. Given the significantly higher FE_{CO} and j_{CO} of Fe–N_5 relative to Fe–N_6, it is safe to conclude that Fe–N_5 had a higher intrinsic activity towards CO_2 electroreduction. To probe the active center and eliminate the interference of the substrate (N-doped porous carbon), we further pyrolyzed pure ZIF-8 at 800 and 900 °C, which was denoted as ZIF-8-800 and ZIF-8-900, respectively (Fig. S10†). It is worth noting that the FE_{CO} of ZIF-8-800 and ZIF-8-900 was lower than 25% (Fig. S11†), demonstrating that Fe atoms in Fe–N_5 and Fe–N_6 are largely responsible for the electroreduction of CO_2 to CO. Moreover, the FE_{CO} of commercial Fe nanoparticles, Fe_3O_4, and Fe_2O_3 were negligible at −0.55 V vs. RHE, demonstrating that atomically distributed Fe sites are the active center rather than bulk Fe species (Fig. S12†). As shown in Fig. 3c, the TOF of CO (TOF_{CO}) was normalized by the mass loading of Fe at different applied potentials. It can be seen that the TOF_{CO} of Fe–N_5 significantly exceeded that of Fe–N_6 throughout the applied potential range. Particularly, for Fe–N_5, the TOF_{CO} reached 5006 h^{-1} at −1.05 V vs. RHE, which was 3.8 times that for Fe–N_6. All these results strongly corroborate the intrinsically higher CO_2 electroreduction performance of Fe–N_5 relative to that of Fe–N_6,

which is comparable to the best reported SACs for CO_2 electroreduction (Table S3†). In view of the excellent selectivity and activity of Fe–N_5 for CO_2 electroreduction, we performed potentiostatic measurements to assess its durability in 1.0 M KOH aqueous solution at −0.4 V vs. RHE. As shown in Fig. 3d, the current density and the FE_{CO} of Fe–N_5 remained basically unchanged during the 24 h continuous electrolysis. TEM and HAADF-STEM images of Fe–N_5 after the stability test show that the Fe single atoms were still atomically dispersed on the N-doped carbon support (Fig. S13†). The N1s XPS spectra of spent Fe–N_5 resembled that of pristine Fe–N_5, indicating the superior stability after the reaction (Fig. S14 and Table S4†).

3.3. Mechanistic studies on CO_2 electroreduction

To further investigate the origin of the intrinsically high electrocatalytic performance of Fe–N_5, we conducted CO_2 temperature-programmed desorption (CO_2-TPD). As shown in Fig. 4a, the CO_2 desorption peak of Fe–N_5 was located at 141 °C, which was higher than that (118 °C) of Fe–N_6. As such, the binding strength of CO_2 on Fe–N_5 was stronger than that on Fe–N_6. The strong binding of CO_2 on Fe–N_5 indicated the facilitated adsorption of CO_2, thus resulting in the high activity of Fe–N_5.[44,45] This is in line with the enhanced CO_2 adsorption on Fe–N_5 compared to that on Fe–N_6 (Fig. S15†). To provide a theoretical insight into the relationship between the coordination number and the reaction pathway, we calculated the Gibbs free energy for each step involved in CO_2 electroreduction (Table S5†). The structural models of Fe–N_5 and Fe–N_6 were established via the obtained XPS and EXAFS fitting results (Table S2 and Fig. S16†). The structural model of Fe–N_6
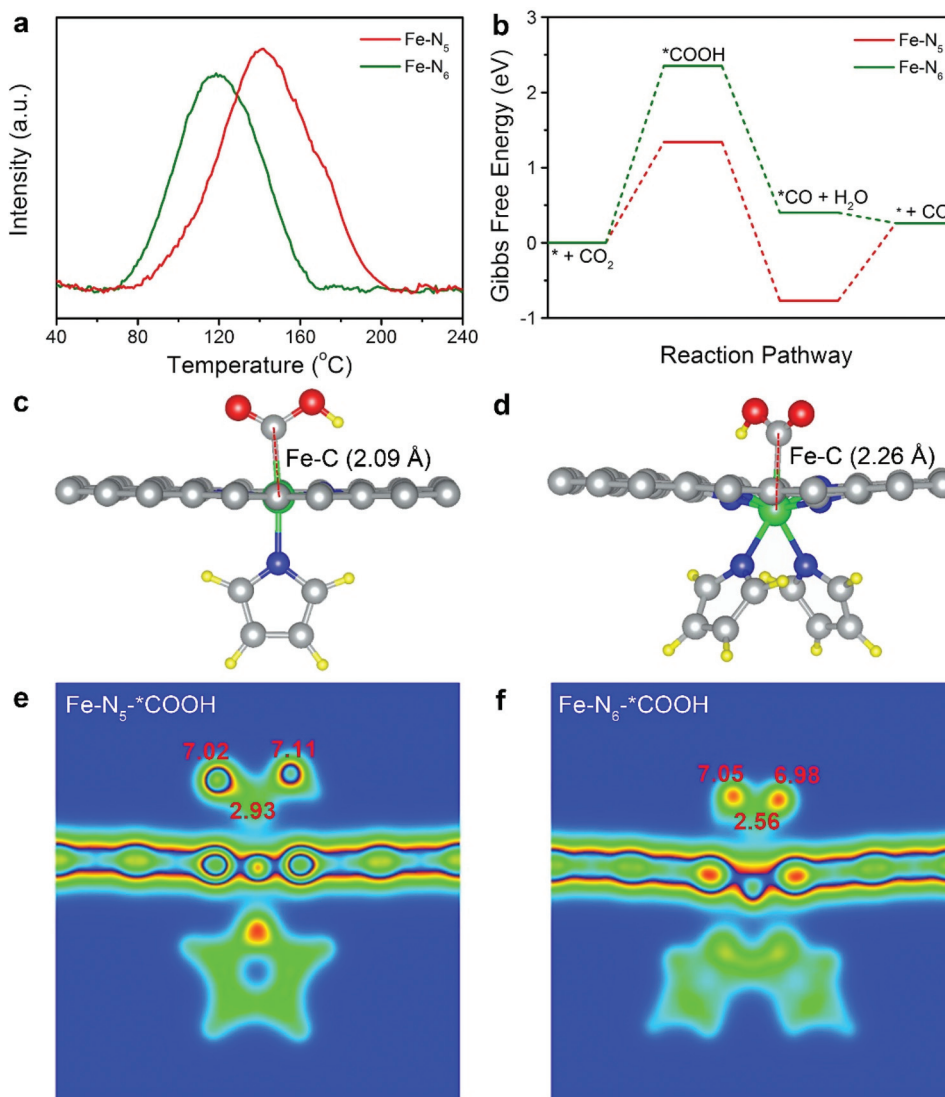
Fig. 4 (a) CO_2-TPD profiles for Fe–N$_5$ and Fe–N$_6$. (b) Calculated Gibbs free energy diagrams for CO_2 electroreduction to CO over Fe–N$_5$ and Fe–N$_6$. (c) and (d) Optimized structures of Fe–N$_5$ and Fe–N$_6$ with adsorbed *COOH, * denotes the adsorption site. The gray, green, blue, red and yellow spheres represent C, Fe, N, O, and H atoms, respectively. (e) and (f) Slice of calculated charge densities of Fe–N$_5$ and Fe–N$_6$ with adsorbed *COOH. Bader partial atomic charges are labeled by the red numbers.

with one pyrrole ring on each side of carbon matrix was excluded after structure optimization (Fig. S17†). As shown in Fig. 4b, the formation of *COOH required the highest energy barrier among all the steps of CO_2 electroreduction on both Fe–N$_5$ and Fe–N$_6$. Therefore, the formation of *COOH serves as the potential-limiting step over Fe–N$_5$ and Fe–N$_6$ towards CO_2 electroreduction. Particularly, the Gibbs free energy for the formation of *COOH on Fe–N$_5$ was 1.34 eV, which was significantly lower than that on Fe–N$_6$ (2.35 eV). As shown in Fig. 4c and d, the C–Fe bond length of adsorbed *COOH for Fe–N$_5$ and Fe–N$_6$ increased from 2.09 to 2.26 Å, respectively, further revealing that Fe–N$_5$ was more beneficial for *COOH adsorption relative to Fe–N$_6$. Apart from that, the C atom of adsorbed *COOH on Fe–N$_5$ displays higher electron density compared to that on Fe–N$_6$, confirming the stronger stabilization of *COOH

on Fe–N$_5$ (Fig. 4e and f).[46] As such, Fe–N$_5$ promoted the activation of CO_2, leading to the enhanced electrocatalytic activity for CO_2 electroreduction relative to Fe–N$_6$.

4. Conclusions

In summary, we have synthesized two Fe SACs for CO_2 electroreduction. Compared with Fe–N$_6$, Fe–N$_5$ demonstrated a lower onset potential (−0.16 V *vs*. RHE), higher turnover frequency (5006 h^{-1}), and remarkable faradaic efficiency (99%) for CO production. This was attributed to the facile adsorption and activation of CO_2 arising from the favourable coordination structure. This work should pave a promising avenue to rationally design novel single-atom electrocatalysts with a tunable

coordination environment in energy and environment related fields.

Conflicts of interest

The authors declare that they have no known competing financial interest or personal relationships that could have appeared to influence the work reported in this paper.

Acknowledgements

References

1 M. Ding, R. W. Flaig, H.-L. Jiang and O. M. Yaghi, *Chem. Soc. Rev.*, 2019, **48**, 2783–2828.

2 A. Goeppert, M. Czaun, G. S. Prakash and G. A. Olah, *Energy Environ. Sci.*, 2012, **5**, 7833–7853.

3 T. Zheng, K. Jiang and H. Wang, *Adv. Mater.*, 2018, **30**, 1802066.

4 J. Qiao, Y. Liu, F. Hong and J. Zhang, *Chem. Soc. Rev.*, 2014, **43**, 631–675.

5 R. Kortlever, J. Shen, K. J. P. Schouten, F. Calle-Vallejo and M. T. Koper, *J. Phys. Chem. Lett.*, 2015, **6**, 4073–4082.

6 D. D. Zhu, J. L. Liu and S. Z. Qiao, *Adv. Mater.*, 2016, **28**, 3423–3452.

7 Y. Chen, C. W. Li and M. W. Kanan, *J. Am. Chem. Soc.*, 2012, **134**, 19969–19972.

8 Z. Geng, X. Kong, W. Chen, H. Su, Y. Liu, F. Cai, G. Wang and J. Zeng, *Angew. Chem., Int. Ed.*, 2018, **57**, 6054–6059.

9 Y. Li and Q. Sun, *Adv. Energy Mater.*, 2016, **6**, 1600463.

10 Z. W. Seh, J. Kibsgaard, C. F. Dickens, I. Chorkendorff, J. K. Nørskov and T. F. Jaramillo, *Science*, 2017, **355**, eaad4998.

11 E. E. Benson, C. P. Kubiak, A. J. Sathrum and J. M. Smieja, *Chem. Soc. Rev.*, 2009, **38**, 89–99.

12 C. G. Margarit, N. G. Asimow, C. Costentin and D. G. Nocera, *ACS Energy Lett.*, 2020, **5**, 72–78.

13 R. Daiyan, X. Tan, R. Chen, W. H. Saputera, H. A. Tahini, E. Lovell, Y. H. Ng, S. C. Smith, L. Dai, X. Lu and R. Amal, *ACS Energy Lett.*, 2018, **3**, 2292–2298.

14 Y. Chen, C. W. Li and M. W. Kanan, *J. Am. Chem. Soc.*, 2012, **134**, 19969–19972.

15 W. Zhu, Y. J. Zhang, H. Zhang, H. Lv, Q. Li, R. Michalsky, A. A. Peterson and S. Sun, *J. Am. Chem. Soc.*, 2014, **136**, 16132–16135.

16 M. Liu, Y. Pang, B. Zhang, P. D. Luna, O. Voznyy, J. Xu, X. Zheng, C. T. Dinh, F. Fan, C. Cao, F. P. G. de Arquer, T. S. Safaei, A. Mepham, A. Klinkova, E. Kumacheva, T. Filleter, D. Sinton, S. O. Kelley and E. H. Sargent, *Nature*, 2016, **537**, 382–386.

17 Y. Chen, S. Ji, Y. Wang, J. Dong, W. Chen, Z. Li, R. Shen, L. Zheng, Z. Zhuang, D. Wang and Y. Li, *Angew. Chem., Int. Ed.*, 2017, **56**, 6937–6941.

18 H. T. Chung, D. A. Cullen, D. Higgins, B. T. Sneed, E. F. Holby, K. L. More and P. Zelenay, *Science*, 2017, **357**, 479–484.

19 L. Fan, P. F. Liu, X. Yan, L. Gu, Z. Z. Yang, H. G. Yang, S. Qiu and X. Yao, *Nat. Commun.*, 2016, **7**, 10667.

20 Y. Xing, J. Ku, W. Fu, L. Wang and H. Chen, *Chem. Eng. J.*, 2020, **395**, 125149.

21 Y.-N. Gong, L. Jiao, Y. Qian, C.-Y. Pan, L. Zheng, X. Cai, B. Liu, S.-H. Yu and H.-L. Jiang, *Angew. Chem.*, 2020, **59**, 2705–2709.

22 L. Liu and A. Corma, *Chem. Rev.*, 2018, **118**, 4981–5079.

23 M. Jia, S. Hong, T.-S. Wu, X. Li, Y.-L. Soo and Z. Sun, *Chem. Commun.*, 2019, **55**, 12024–12027.

24 E. Zhang, T. Wang, K. Yu, J. Liu, W. Chen, A. Li, H. Rong, R. Lin, S. Ji and X. Zheng, *J. Am. Chem. Soc.*, 2019, **141**, 16569–16573.

25 W. Ren, X. Tan, W. Yang, C. Jia, S. Xu, K. Wang, S. C. Smith and C. Zhao, *Angew. Chem., Int. Ed.*, 2019, **58**, 6972–6976.

26 C. Zhang, S. Yang, J. Wu, M. Liu, S. Yazdi, M. Ren, J. Sha, J. Zhong, K. Nie and A. S. Jalilov, *Adv. Energy Mater.*, 2018, **8**, 1703487.

27 X. Wang, Z. Chen, X. Zhao, T. Yao, W. Chen, R. You, C. Zhao, G. Wu, J. Wang, W. Huang, J. Yang, X. Hong, S. Wei, Y. Wu and Y. Li, *Angew. Chem., Int. Ed.*, 2018, **57**, 1944–1948.

28 K. Mou, Z. Chen, X. Zhang, M. Jiao, X. Zhang, X. Ge, W. Zhang and L. Liu, *Small*, 2019, **15**, 1903668.

29 Y. Chen, S. Ji, C. Chen, Q. Peng, D. Wang and Y. Li, *Joule*, 2018, **2**, 1242–1264.

30 X. Su, X.-F. Yang, Y. Huang, B. Liu and T. Zhang, *Acc. Chem. Res.*, 2018, **52**, 656–664.

31 X. Rong, H.-J. Wang, X.-L. Lu, R. Si and T.-B. Lu, *Angew. Chem.*, 2020, **59**, 1961–1965.

32 C. Zhao, X. Dai, T. Yao, W. Chen, X. Wang, J. Wang, J. Yang, S. Wei, Y. Wu and Y. Li, *J. Am. Chem. Soc.*, 2017, **139**, 8078–8081.

33 N. Leonard, W. Ju, I. Sinev, J. Steinberg, F. Luo, A. S. Varela, B. R. Cuenya and P. Strasser, *Chem. Sci.*, 2018, **9**, 5064–5073.

34 H. Zhang, J. Li, S. Xi, Y. Du, X. Hai, J. Wang, H. Xu, G. Wu, J. Zhang, J. Lu and J. Wang, *Angew. Chem., Int. Ed.*, 2019, **58**, 14871–14876.

35 J. Gu, C.-S. Hsu, L. Bai, H. M. Chen and X. Hu, *Science*, 2019, **364**, 1091–1094.

36 H. Zhang, S. Hwang, M. Wang, Z. Feng, S. Karakalos, L. Luo, Z. Qiao, X. Xie, C. Wang and D. Su, *J. Am. Chem. Soc.*, 2017, **139**, 14143–14149.

37 V. Strauss, K. Marsh, M. D. Kowal, M. El-Kady and R. B. Kaner, *Adv. Mater.*, 2018, **30**, 1704449.

38 Z. Ma, C. Tsounis, P. V. Kumar, Z. Han, R. J. Wong, C. Y. Toe, S. Zhou, N. M. Bedford, L. Thomsen and Y. H. Ng, *Adv. Funct. Mater.*, 2020, **30**, 1910118.

39 M. Ma, K. Liu, J. Shen, R. Kas and W. A. Smith, *ACS Energy Lett.*, 2018, **3**, 1301–1306.

40 C. Kim, T. Eom, M. S. Jee, H. Jung, H. Kim, B. K. Min and Y. J. Hwang, *ACS Catal.*, 2017, **7**, 779–785.

41 S. Zhao, R. Jin and R. Jin, *ACS Energy Lett.*, 2018, **3**, 452–462.

42 Y. S. Ham, S. Choe, M. J. Kim, T. Lim, S. K. Kim and J. J. Kim, *Appl. Catal., B*, 2017, **208**, 35–43.

43 S. M. Lee, H. Lee, J. Kim, S. H. Ahn and S. T. Chang, *Appl. Catal., B*, 2019, **259**, 118045.

44 Z. Geng, Y. Cao, W. Chen, X. Kong, Y. Liu, T. Yao and Y. Lin, *Appl. Catal., B*, 2019, **240**, 234–240.

45 J. Zhang, R. Yin, Q. Shao, T. Zhu and X. Huang, *Angew. Chem., Int. Ed.*, 2019, **58**, 5609–5613.

46 F. Y. Gao, S. J. Hu, X. L. Zhang, Y. R. Zheng, H. J. Wang, Z. Z. Niu, P. P. Yang, R. C. Bao, T. Ma and Z. Dang, *Angew. Chem.*, 2020, **132**, 8784–8790.